Direct Single-Enzyme Biomineralization of Catalytically Active Ceria and Ceria−Zirconia Nanocrystals

Christopher D. Curran,[†] Li Lu,[‡] Yue Jia,[†] Christopher J. Kiely,[†,‡] Bryan W. Berger,[*,†,§] and Steven McIntosh[*,†]

[†]Department of Chemical and Biomolecular Engineering and [§]Program in Bioengineering, Lehigh University, 111 Research Drive, Bethlehem, Pennsylvania 18015, United States

[‡]Department of Materials Science and Engineering, Lehigh University, 5 East Packer Avenue, Bethlehem, Pennsylvania 18015, United States

* Supporting Information

ABSTRACT: Biomineralization is an intriguing approach to the synthesis of functional inorganic materials for energy applications whereby biological systems are engineered to mineralize inorganic materials and control their structure over multiple length scales under mild reaction conditions. Herein we demonstrate a single-enzyme-mediated biomineralization route to synthesize crystalline, catalytically active, quantum-confined ceria (CeO_{2-x}) and ceria−zirconia ($Ce_{1-y}Zr_yO_{2-x}$) nanocrystals for application as environmental catalysts. In contrast to typical anthropogenic synthesis routes, the crystalline oxide nanoparticles are formed at room temperature from an otherwise inert aqueous solution without the addition of a precipitant or additional reactant. An engineered form of silicatein, rCeSi, as a single enzyme not only catalyzes the direct biomineralization of the nanocrystalline oxides but also serves as a templating agent to control their morphological structure. The biomineralized nanocrystals of less than 3 nm in diameter are catalytically active toward carbon monoxide oxidation following an oxidative annealing step to remove carbonaceous residue. The intro-duction of zirconia into the nanocrystals leads to an increase in Ce(III) concentration, associated catalytic activity, and the thermal stability of the nanocrystals.

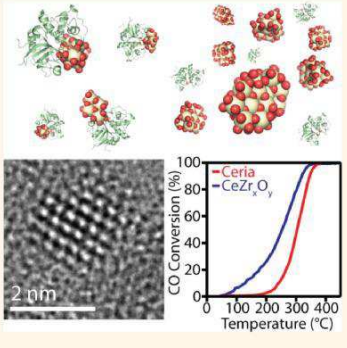

KEYWORDS: biomineralization, ceria, ceria−zirconia, nanoparticle, solid solution, catalysis, CO oxidation

Ceria and ceria−zirconia nanoparticles are of functional interest due to their current widespread commercial application in environmental catalysis[1] and their use in fuel cells,[2] as pharmacological agents,[3] and chemical mechanical planarization abrasives.[4] Ceria and ceria−zirconia mixed oxides are widely utilized in automotive exhaust catalysis as oxygen storage materials due to the facile redox behavior that exists between Ce(III) and Ce(IV). This facile redox couple also makes ceria-based materials active oxidation catalysts and catalyst supports for a wide range of oxidation reactions.[5−7] The intro-duction of zirconia into ceria enhances the formation of oxygen defects within the nanocrystals to promote catalytic activity and also increases the thermal stability of the materials.[8,9] Ceria and ceria−zirconia nanomaterials are most commonly synthesized by flame pyrolysis,[10] co-precipitation,[11] or hydrothermal routes,[12] which all require elevated temperatures and, most typically, the use of a base to induce precipitation from the precursor solu-tion. Biomineralization seeks to utilize biological systems as potentially green and scalable alternatives to typical material synthesis routes. Our primary goal in this work is to demonstrate that biomineralization is a feasible, green, pathway to the formation of ceria and ceria−zirconia nanoparticles and that these bio-mineralized materials are functionally equivalent to their chemi-cally synthesized counterparts.

Natural biomineralization pathways[13,14] most commonly form amorphous structural materials, for example, calcium carbonate-biopolymer composite mollusk shells,[15] iron oxides in the teeth of limpets,[16] or structural spicules of silica in sea sponges.[17] Mann, in his classic textbook, categorized biomineralization into either biologically induced mineralization, whereby mineralization occurs through a metabolic reaction of precursors in solution, or biologically controlled mineralization, whereby the biological system controls the structure of the mineral, but the mineraliza-tion process occurs through supersaturation rather than a metabolic turnover of precursors.[18] Without structural control, biologically induced mineralization leads to materials with irregular size, shape, structure, and composition, making such an approach generally unfavorable for the formation of well-defined

functional nanomaterials. In contrast, a reliance only on precipitation from a supersaturated solution limits the materials palette available to thermodynamically favorable products unless, as in a biotemplating approach, an additional reactive chemical species is introduced, e.g., in functional material production, the use of Na_2S as a reactive sulfur source in CdS biomineralization[19] and H_2O_2 as an oxidizing agent in Co_3O_4 biomineralization for battery applications.[20] The challenge to producing "green" functional materials by biomineralization is thus to develop approaches that combine metabolic or, more generally, active enzymatic precursor turnover with biotemplating in a single biological system; we term this combination direct biomineralization. Herein, we demonstrate a single enzyme active for the direct biomineralization of cerium oxide and cerium−zirconium oxide solid solution nanoparticles. To the best of our knowledge, there are no prior reports of direct biomineralization of these widely utilized catalytic materials, nor are there prior reports of biomineralized oxide materials being used as active heterogeneous catalysts for gas phase reactions.

Templated biomineralization of ceria has previously been reported by Okuda et al., who utilized an apoferritin cage to template CeO_2 nanoparticles upon inducing mineralization with HEPES−NaOH in aqueous solution.[21] This process yields nanoparticles ~5 nm in size but requires multiple separation steps to remove larger "bulk" ceria particles formed through reaction of the precipitant with free ceria, that is, ceria precursor in solution that is not associated with a templating ferritin cage. In contrast, the combined enzymatic mineralization and templating approach described herein exclusively produces ceria nanocrystals, and no subsequent particle size selection is required.

The motivation for the current direct biomineralization work comes from our previous work developing a single enzyme for direct sulfide biomineralization[22] and the fascinating reports regarding silicateins, silica proteins, first identified by Shimizu et al. as responsible for biomineralization of silica spicules in the marine sponge Tethya aurantia.[23] These silicateins assemble into axial filaments and actively turn over a precursor, most likely silicic acid, in the ocean to form largely amorphous hydrated silica spicules in sea sponges. The amino acid sequences of the most abundant silicateins isolated from Tethya aurantia (α- and β-forms) are very similar (50% by sequence, up to 75% by function) to the well-studied cathepsin-L family of hydrolytic enzymes, suggesting a mechanistic pathway to silica from the tetraethylorthosilicate precursor via hydrolysis of ligands surrounding the precursor.[24] For a full discussion of the use of silicatein in inorganic material synthesis we refer the reader to the excellent review by Andre et al.[25]

Native or recombinant forms of silicatein have previously been successfully applied to biomineralization of silicon dioxide,[24] titanium dioxide,[26] gallium(III) oxide,[27] tin dioxide,[28] and barium titanate oxyfluoride[29] particles. This body of work is complemented by that of the Tremel group, who have sought to utilize surface-immobilized silicatein to mineralize thin films of multiple materials onto inorganic support materials.[28,30−32] Of particular relevance to the current work is the pursuit of biomineralized functional materials. One particular challenge in this area is the balance of crystalline versus amorphous structure formed during mineralization, as typically the crystalline phase is the desirable component for functional activity. For example, silicatein biomineralization of both titanium dioxide and zirconium dioxide is reported to lead to the formation of relatively sparse nanocrystalline domains within largely amorphous matrices,[30,31] and crystalline γ-Ga_2O_3 is formed only at very low precursor concentration.[27] In the pursuit of highly crystalline materials, Bawazer et al. developed an engineered recombinant form of silicatein that is active in the formation of ~5 nm partially crystalline titania, demonstrating a critical link between enzyme sequence and nanoparticle crystallinity.[33] In contrast, $BaTiOF_4$ was successfully biomineralized in crystalline form, although unfortunately without any corresponding functional property measurements, most likely due to the relatively low material yield of many biomineralization strategies; the authors in that work note that insufficient material was obtained for X-ray diffraction (XRD) analysis.[29]

While the pursuit of functional materials is ongoing, there are, to the best of our knowledge, no prior reports of the functional properties of directly biomineralized catalytic oxides, although there are some reports regarding the function of other directly biomineralized materials, for example, the use of directly bio-mineralized metal chalcogenide quantum dots in photovoltaic applications,[34] the magnetic properties of fungi-mediated biomineralized magnetite,[35] the ferroelectric properties of fungi-mediated barium titanate,[36] and reports of fungi-mediated manganese-containing materials,[37] or bacterial-mediated γ-FeOOH to form α-Fe_2O_3 base Li-ion battery electrodes upon a brief heat treatment.[38]

RESULTS AND DISCUSSION

Herein we describe the single-enzyme direct biomineralization of ceria and ceria−zirconia solid solution nanocrystals of less than 3 nm diameter from an aqueous solution of cerium(IV) ammonium nitrate and zirconium(IV) dinitrate oxide. Nano-crystal biomineralization of the oxides occurs without the addition of any reducing agent or additional templating species or any postmineralization heating. The resulting nanocrystals are demonstrated as active catalysts for carbon monoxide oxidation, one of a large number of potential energy and environmental catalysis applications ranging from water gas shift catalysts, to promoters in automotive three-way catalysts, to oxidation catalysts for direct hydrocarbon solid oxide fuel cells. Herein, we demonstrate single-enzyme-mediated direct biomineraliza-tion of crystalline ceria nanoparticles, the direct biomineraliza-tion of solid solution ceria−zirconia crystalline nanoparticles, and the catalytic activity of the biomineralized materials.

We have engineered a form of recombinant ceria-mineralizing silicatein from Petrosia f iciformis (NCBI accession number Q6YD92.1) denoted hereafter as rCeSi, by taking the wild-type sequence and generating serial truncations of the N- and C-terminal to improve expression yield from E. coli. We identified a truncated sequence containing amino acids 124−217 as well as a C-terminal hexahistidine tag that exhibited consistently high expression from E. coli (rCeSi). Previous studies to engineer silicatein have used DNA shuffling to diversify silicatein sequences as well as including C-terminal hexahistidine tags.[33]

Incubation of the rCeSi enzyme with an aqueous cerium(IV) ammonium nitrate (CAN) precursor solution for 24 h led to the formation of an opaque, yellow solution, showing laser light scattering properties consistent with the formation of a colloid, Figure 1a and b. No corresponding color change or colloid formation was observed for the control samples, which were identical in composition and synthesis conditions to the primary samples except that no rCeSi was added, Figure 1a and b. Aqueous CAN solutions are shelf-stable and do not undergo spontaneous oxidation to form nanocrystals within this time period at this temperature and pH. XRD patterns collected in our

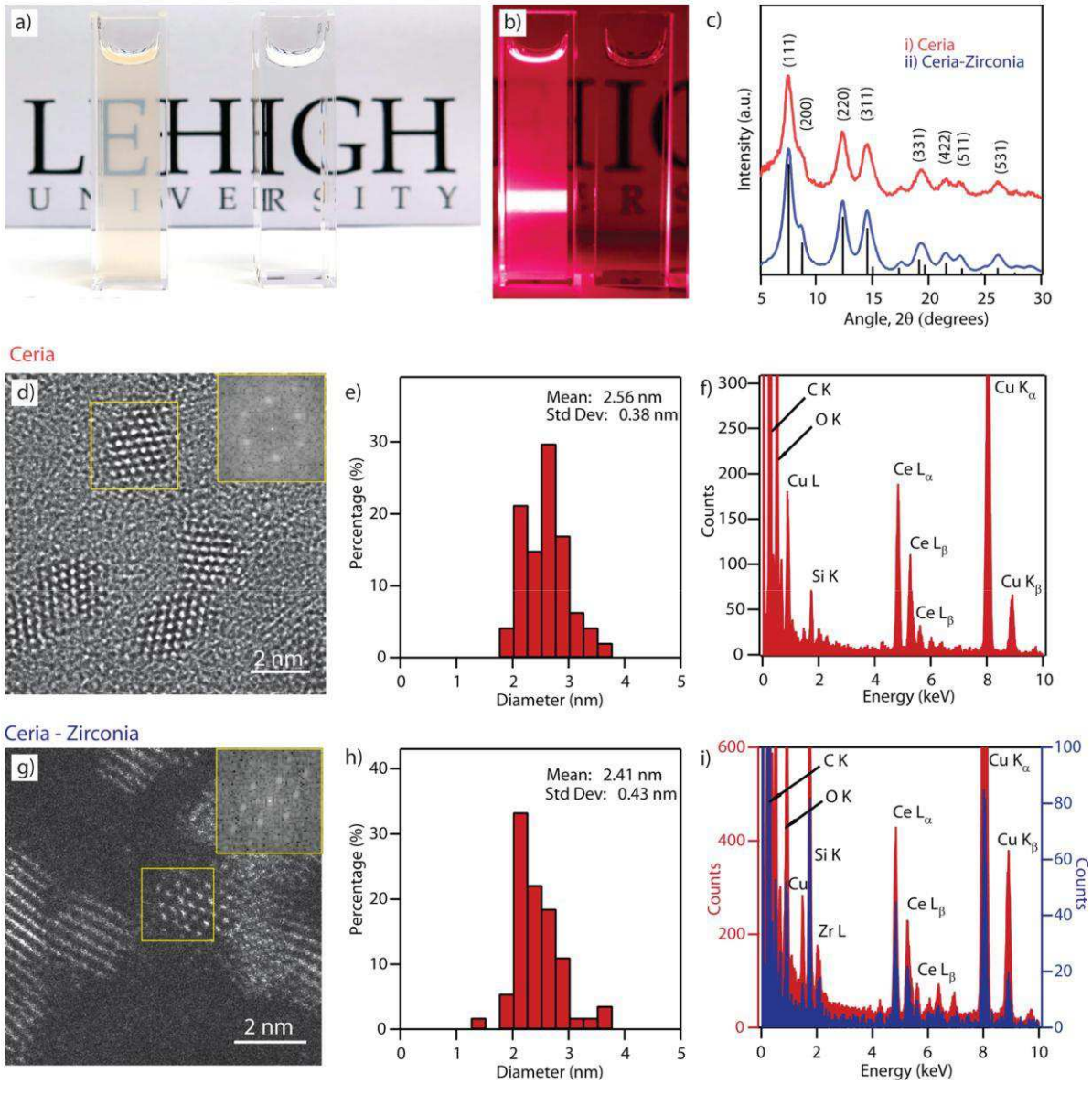

Figure 1. Ceria and ceria−zirconia nanocrystal biomineralization. (a) Photograph under natural light and (b) photograph with red laser illumination of cerium(IV) ammonium nitrate precursor incubated with rCeSi (left) and without rCeSi (right). An opaque, pale yellow sol is formed in the presence of rCeSi enzyme but not in the control sample, which shows no precipitation or color change. The laser light scattering demonstrates the presence of colloidal particles in the sample with rCeSi enzyme and no particles in the sample without rCeSi. The laser beam is coming from the right and is passing through both sample vials. (c) Synchrotron powder X-ray diffraction spectra of the dried as-synthesized product of incubation of (i) rCeSi with the cerium(IV) ammonium nitrate and (ii) rCeSi with a 1:1 molar mixture of cerium(IV) ammonium nitrate and zirconium(IV) dinitrate oxide (ICSD collection code 156250, substantial peaks identified). (d) Representative HRTEM image of as-synthesized ceria nanocrystals; the inset fast Fourier transform (FFT) from the particle in the yellow box is consistent with the $[1\bar{1}0]$ projection of the CeO_2 (fluorite) structure. (e) Corresponding spherical equivalent particle size distribution, with no particles larger than 4 nm being observed. (f) XEDS spectrum confirming the presence of Ce and O in the particles. The Cu and C signals originate from the TEM grid, and the Si signal is an artifact from the Si drift detector. (g) HAADF-STEM image of the as-synthesized ceria−zirconia particles; the inset FFT obtained from the particle in the yellow box is consistent with the $[1\bar{1}0]$ projection of the fluorite structure. (h) Corresponding spherical equivalent particle size distribution for the ceria−zirconia sample. (i) XEDS spectrum from a single nanoparticle (blue) and the summation of 10 spectra from extended area nanocrystal groupings (red), confirming the presence of both Ce and Zr in the nanocrystals. Logo in images a and b credited to Lehigh University.

laboratory can be indexed to the fluorite structure of ceria and are consistent between batches, Figure S1.

The synchrotron XRD pattern, shown in Figure 1c, of the solid pellet centrifuged from this opaque solution shows peak positions and peak broadening consistent with the formation of CeO_2 nanoparticles having the fluorite structure (ICSD collection code 156250). Rietveld refinement, Figure S2, of the XRD pattern confirms the fluorite structure, space group $Fm\bar{3}m$, with a lattice parameter of 5.449(1) Å and mean crystallite size, estimated from the Lorentzian crystallite size broadening parameter as implemented in GSAS,[39] of 22.1 ± 0.2 Å.

Figure 1d shows a high-resolution transmission electron microscopy (HR-TEM) image of the centrifuged and dried pure ceria sample, demonstrating that the ceria has been mineralized

as highly faceted individual crystalline nanoparticles. The interplanar spacings and angles present in these phase contrast images are in good agreement with those expected for the fluorite structure of CeO_2, Figure S3. The ceria nanoparticles have a tight size distribution with mean particle diameter (based on area equivalent spherical particles) of 2.56 ± 0.38 nm, Figure 1e, which is consistent with the crystallite size estimated from XRD. No large crystallites or amorphous regions were observed during imaging of multiple samples. Furthermore, X-ray energy dispersive spectroscopy (XEDS) analysis confirms the presence of only cerium and oxygen within the particles, Figure 1f. While there is likely residual carbonaceous material, including the enzyme, in the as-prepared sample, the particles do not appear to be bound within any carbonaceous matrix and are stable as a colloid upon resuspending in dilute nitric acid without any additional processing.

Thus, the protein biologically induces ceria mineralization, in contrast to biologically templating during chemically induced mineralization.[21] It is especially important to note that, unlike other preparation methods, ceria nanocrystal formation occurs in aqueous solution without the addition of a base or elevation of temperature and in the absence of an explicit chemical structure-directing agent. Furthermore, these ceria nanoparticles are among the smallest reported in the literature.[40,41] The ability to form such small particles is a consequence of the direct biomineralization of the material. The majority of chemical approaches to ceria nanoparticle synthesis utilize elevated temperatures during synthesis or during a postannealing step to form the crystalline oxide.[6] While we utilize an annealing step to remove any carbonaceous material prior to catalytic testing, elevated temperature is not required to form the crystalline oxide.

Attempts to biomineralize pure zirconia from zirconium(IV) dinitrate oxide (ZDO) via rCeSi leads to the formation of a solid zirconia phase; however, the product consists primarily of slightly larger (5−10 nm) highly disordered particles with only a relatively few highly crystalline tetragonal zirconia nanoparticles present, Figure S4. This is similar to prior reports of amorphous silicon dioxide,[24] titanium dioxide,[26] and gallium(III) oxide.[27] In contrast, incubation of rCeSi with a 1:1 mixture of CAN and ZDO leads to the formation of an opaque sol after 24 h.

As with the pure ceria sample, XRD patterns of the centrifuged material obtained from this mixed CAN and ZDO solution can be indexed to the fluorite structure of ceria and are consistent between batches, Figure S1. The higher resolution synchrotron XRD pattern of the centrifuged solid material, Figure 1c, is also consistent with the formation of single phase fluorite structured nanoparticles, space group $Fm\bar{3}m$. Rietveld refinement, Figure S2, provides a lattice parameter of 5.437(2) Å and average crystallite size, again from the Lorentzian isotropic size broadening, of 24.53 ± 0.1 Å. When compared with the values obtained for the pure ceria sample, the measured contraction in lattice parameter is consistent with formation of a ceria−zirconia solid solution.[8,42,43]

HAADF-STEM analysis, Figure 1g, again confirms the formation of individual crystalline nanoparticles and the absence of any larger particles or amorphous material (see also Figure S5). The particles have a narrow size distribution, Figure 1h, with a mean size of 2.41 ± 0.43 nm, which is in good agreement with that deduced from XRD.

Compositional analysis of individual nanoparticles by XEDS was attempted, but in many cases we were unable to collect a statistically significant number of X-rays before the nanoparticle was irretrievably damaged by the electron beam. Instead XEDS spectra could be more reliably collected from groups of two or three particles, and analyses on many such NP groupings provided similar XEDS spectra. Figure 1i shows an XEDS spectrum derived from the summation of 10 such "extended area" spectra and one example from an individual nanoparticle. This semiaveraging analysis method supports the conclusion that ceria−zirconia solid solution nanoparticles are formed by incu-bation of rCeSi in the presence of both Ce- and Zr-containing precursors. The relative atomic concentration of Ce:Zr, calculated using a Cliff−Lorimer-type analysis, was determined to be approximately 82%:18%. These biomineralized ceria− zirconia solid solution nanoparticles are among the smallest reported to date.[44]

Interestingly, when the nominal ratio of zirconium to cerium was increased in the synthesis procedure by adjusting the precursor concentrations, their relative atomic concentration of the nanoparticles remained unchanged. Samples synthesized with nominal Ce:Zr ratios, 1:2 and 1:4 in solution, at the same total precursor concentration as the other materials in this study, yield particles with atomic ratios of 83:17 and 81:19, respectively, as determined by XEDS analysis, Figure S6. This lack of sensitivity to increased Zr content in the solution may be due to the intrinsic enzymatic biomineralization turnover kinetics of cerium versus zirconium that is not substantially influenced within the current range of precursor concentrations explored to date. It should certainly be feasible to increase the zirconium content in fluorite structured nanoparticles as demonstrated for chemically synthesized materials.[45,46]

These results unequivocally demonstrate that rCeSi is active to biologically induce and control mineralization of crystalline pure ceria, pure zirconia, and mixed cerium−zirconium oxide nanoparticles under ambient conditions. The catalytic mecha-nism of both ceria and zirconia biomineralization by rCeSi is likely to be similar to that previously proposed for native silicatein, as the proposed catalytic residues of silicatein are preserved in the rCeSi enzyme.[17] The resultant rCeSi from N- and C-terminal truncations is similar to the mature, protease-resistant fragment of P. f iciformis silicatein isolated directly from spicules.[47] While the exact structure of the CAN precursor in solution is still the topic of some debate, most recent studies conclude that it exists as a dimeric entity with bridging Ce−O−Ce bonds.[48,49] The nature of the six-coordinating species around each cerium atom in this dimeric entity varies between reports, possibly due to the variations in the solvent pH employed, but for simple dissolution of the precursor in water, the coordinating species are likely to be a mixture of $(NO_3)^-$, OH^-, and H_2O.[48] In Figure 2 we suggest a hydrolysis mechanism analogous to that proposed previously for biomineralized silica,[24] titania,[26] and gallium oxide[27] using silicatein. Variations in the nature or number of the coordinating ligands surrounding the Ce−O−Ce dimeric structure in the solvated precursor will alter the number of hydrolysis steps required to form the oxide. Interestingly, attempts in our laboratory to utilize a Ce(III)-type precursor, Ce(III) nitrate, did not lead to any observable mineralization, further indicating that the structural state of the precursor in solution is critical to the mineralization mechanism.

This proposed mechanism, whereby a serine and histidine pair within the enzymatic active site form an acid/base pair to catalyze hydrolysis of the precursor, draws upon the sequence and structural similarities between the α-form of native silicatein and the hydrolytic enzyme cathepsin L.[24] This has been exper-imentally demonstrated for tetraorthosilicate hydrolysis by observing a removal of function through site-directed mutagenesis

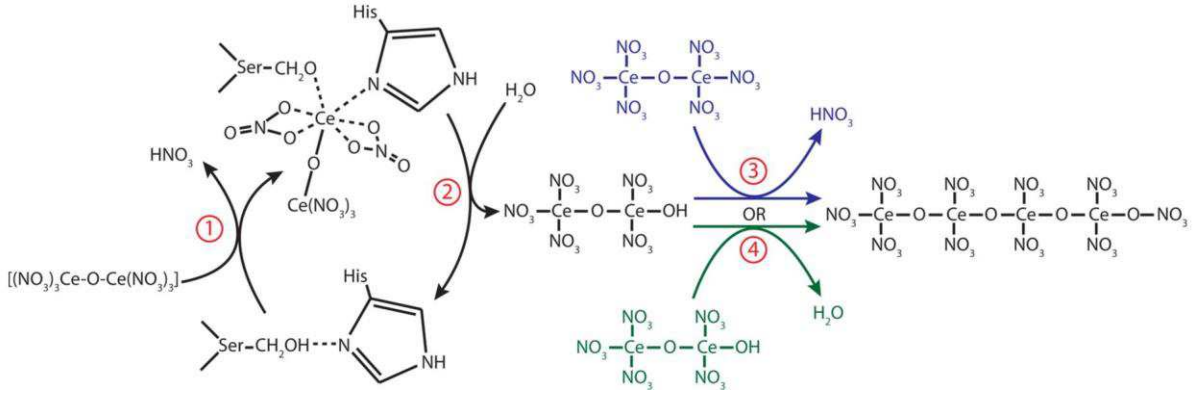

Figure 2. Proposed mechanism for the formation of cerium dioxide nanocrystals from cerium ammonium nitrate: (1) dissociative binding of the precursor to the active site of rCeSi, (2) hydrolysis of the precursor, and either (3) subsequent condensation of a precursor molecule and a hydrolyzed molecule or (4) dehydration of two hydrolyzed precursor species.

to replace either the purported active serine histidine or serine residue with alanine[50] and has been indicated as the mechanism for gallium hydroxide and gallium oxide biomineralization from gallium nitrate.[27] In our case, the hydrolyzed precursor subsequently undergoes condensation or nitrate removal to form ceria. The formation of crystalline ceria, rather than crystalline cerium hydroxide or an amorphous phase, we hypothesize is templated by hydrogen-bonding interactions between hydroxyls on the rCeSi and the hydrolyzed precursors; again this mineralizing and templating mechanism has been proposed for the native silicatein in the biomineralization of silica,[17,24] titania,[26] and gallium oxide.[27]

Unlike the case of pure zirconia, we find no evidence of particles larger than 4 nm or amorphous regions in the ceria or ceria−zirconia materials, further demonstrating an intimate interaction between the two elements rather than independent mineralization of ceria and zirconia. The observed specificity of rCeSi toward templated biomineralization of purely crystalline materials only for ceria-rich compositions is perhaps unsurprising given the previously demonstrated need to engineer material-specific variants to selectively biomineralize crystalline silica or titania.[33] This is particularly true given that the commonly observed crystal structures of zirconia are either monoclinic or tetragonal, whereas those for ceria and ceria-rich ceria−zirconia mixed oxides are both cubic.

Both polyhedral and cuboid particle shapes were found in the biomineralized ceria nanocrystals (see Figure 3), with the polyhedral being the dominant shape. The exposure of {111}-and {200}-type surface facets results in a polyhedral shape, while predominant {200} facet terminations form cuboid-like nanocrystals. These morphologies are consistent with those found in comparable materials synthesized via traditional chemical routes at elevated temperature,[51] indicating that while rCeSi clearly both induces and controls ceria biomineralization, it does not template in such a way to produce surface facet distributions that deviate from the typically expected distribution. As with chemically synthesized nanocrystals, the polyhedral shape is more commonly observed in the biomineralized materials due to the comparable surface energies of the {111} and {200} facets.[51] In common with the ceria nanoparticles, polyhedral and cuboid shapes were also found in the biomineralized ceria−zirconia samples, with the polyhedral shape being dominant.

The Ce−O bond within the fluorite structure is Raman active, with an expected peak position for pure ceria of ~462 cm^{-1}.[52,53] Formation of a ceria−zirconia solid solution shifts this Ce−O bond vibrational frequency to a higher wavenumber.[52−54] Figure 4a shows the Raman spectra for the as-synthesized, non-heat-treated, biomineralized ceria and ceria−zirconia and the purchased commercial pure ceria reference sample. Both the biomineralized and commercial pure ceria show peaks at the expected position of 467 cm^{-1}. In contrast, the peak position of the biomineralized ceria−zirconia is shifted to 480 cm^{-1}, providing further confirmation of the formation of ceria−zirconia solid solution nanoparticles by the enzyme in the aqueous phase at ambient temperature.

Cerium is found in both the 3+ and 4+ oxidation state, as shown in the XPS spectrum presented in Figure 4b. XPS peaks are labeled U and V, following the naming convention set by Burroughs et al., representing the spin−orbit doublet $3d_{5/2}$ and $3d_{3/2}$ respectively.[55] The peaks u, v, u″, v″, u‴, and v‴ correspond to cerium in the 4+ oxidation state, where the u‴ and v‴ result from the $Ce3d^9$ $O2p^6$ $Ce4f^0$ final state, and u, v, u″, and v″ result from a mixing of the $Ce3d^9$ $O2p^5$ $Ce4f^1$ and $Ce3d^9$ $O2p^4$ $Ce4f^2$ final states.[56] The peaks designated u^0, v^0, u′, and v′ correspond to cerium in the 3+ oxidation state, whereas u^0, v^0, u′, and v′ peaks result from a mixing of the $Ce3d^9$ $O2p^5$ $Ce4f^2$ and $Ce3d^9$ $O2p^6$ $Ce4f^1$ final states.[56] Annealing the samples in air leads to an increased Ce(III) content (26%) in the ceria−zirconia sample as compared to pure ceria material (12%). This increased Ce(III) concentration is consistent with previous reports.[8,57] Incorporation of zirconium into the ceria lattice has been shown to reduce the oxygen vacancy formation energy and stabilize oxygen vacancies, leading to a shift in the ceria redox equilibrium and an associated increase in Ce(III) concentration.[58] The determined Ce(III) concentration is within the range of previous reports.[59−61] X-ray photoelectron spectroscopy (XPS) analysis of the Zr(3d) region (see Figure S7) further confirms the presence of the zirconium in the mixed sample and suggests it exists solely in the 4+ oxidation state.

The direct optical band gap for our biomineralized ceria and ceria−zirconia materials and a commercial sample containing 15−30 nm ceria nanoparticles were determined to be 3.55(3), 3.57(3), and 3.22(3) eV, respectively, Figure 5a. The significant increase in band gap for the biomineralized ceria compared with the commercial ceria material is consistent with expectations and prior reports of quantum confinement in similarly sized chemically synthesized ceria nanocrystals.[62] A simplistic type of Vegard's law relationship has been shown to apply to the band gap of some alloy semiconductors.[63] All other things being equal, increasing the zirconium content in ceria should have the effect of

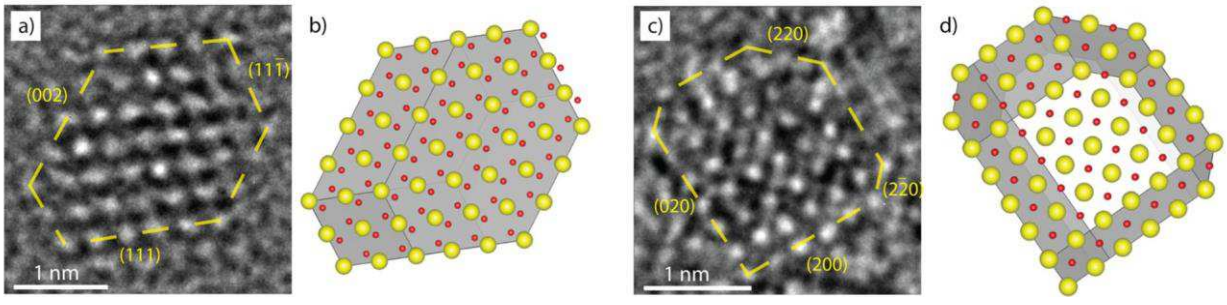

Figure 3. Faceting of biomineralized ceria nanocrystals. Representative (a and c) HR-TEM images of biomineralized ceria having polyhedral and truncated cubic morphology nanocrystals; (b and d) plausible schematic reconstructions of the NPs shown in (a) and (c), respectively. The polyhedral nanocrystals are the more abundant entities.

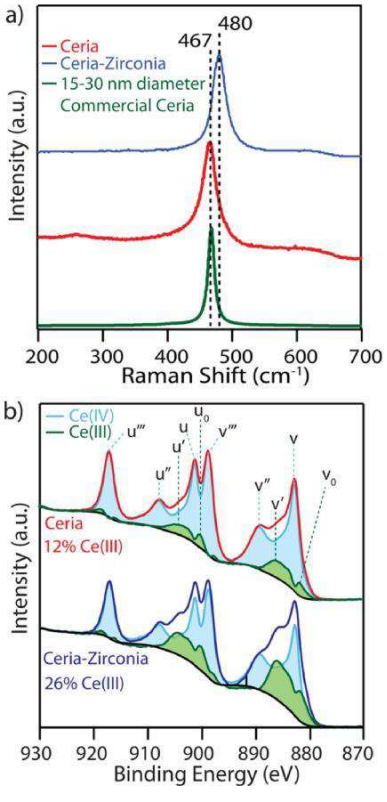

Figure 4. Raman and X-ray photoelectron spectroscopic analysis. (a) Raman spectra collected on as-prepared samples of biomineralized ceria and ceria−zirconia and from the commercially obtained reference sample of ceria. The increase in measured Raman shift for the ceria−zirconia sample is consistent with the formation of a solid solution. (b) X-ray photoelectron spectra of the Ce(3d) region of the biomineralized ceria and ceria−zirconia samples following annealing of both powders in air at 500 °C for 20 min, demonstrating the increased Ce(III) concentration, and thus higher oxygen defect concentration, upon doping with zirconia.

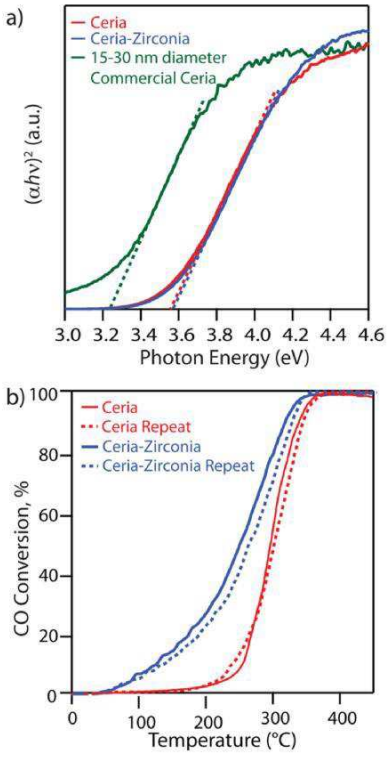

Figure 5. Optical properties and catalytic activity toward CO oxidation: (a) optical band gap determination for the as-synthesized biomineralized ceria and ceria−zirconia nanocrystals compared to larger grained (15−30 nm) commercially purchased ceria. The increase in band gap is indicative of the quantum confinement of the <3 nm diameter biomineralized nanocrystals. (b) CO conversion as a function of temperature for comparing the catalytic activity of biomineralized ceria and ceria−zirconia nanoparticles. The temper-ature required to achieve 50% conversion for the ceria sample is 304 °C, whereas that for the ceria−zirconia material is 252 °C. This reduction in temperature is a consequence of the enhanced reducibility and increased thermal stability of the ceria material upon incorporation of zirconium atoms within the structure. Data for a second repeat of the light-off measurement on the same sample is included.

increasing the band gap, due to the band gap of bulk cubic zirconia being 6−7 eV.[64] However, prior literature has shown that an increase in Ce(III) concentration in $Ce_{1-y}Zr_yO_{2-x}$, along with the associated increase in oxygen vacancy concentration, leads to the formation of a partially occupied $4f^1$ band that reduces the band gap of oxygen deficient ceria.[65,66] As shown in Figure 4b, there is a significant increase in Ce(III) concentration upon zirconia incorporation. Therefore, the lack of measured band gap increase upon Zr doping that may be predicted from a simple Vegard's law approach is most likely due to the opposing influence of increased oxygen vacancy concentration. In addition, numerous subtle factors including influence of chemical environment and capping ligands can potentially influence the measured band gap.

The underlying motivation for introducing zirconium atoms into ceria is to enhance the thermal stability, oxygen storage capacity, and associated catalytic activity of the material relative to that of pure ceria. Hence, CO oxidation was chosen as a simple test reaction to characterize the catalytic performance of our

biomineralized materials. CO light-off curves, presented in Figure 5b, demonstrate enhanced activity of the biomineralized ceria−zirconia sample through a 52 °C reduction in the temperature (from 304 ± 5 °C down to 252 ± 5 °C) to achieve 50% CO conversion. For comparison, commercial ceria (Alfa Aesar, 15−30 nm), under identical reaction conditions, exhibited a 50% conversion at 293 ± 5 °C, which is in reasonable agreement with the light-off data for our biomineralized pure ceria nanoparticles. Repetition of the experiment utilizing the same sample showed very little shift in the light-off curve, indicating the stability of our biomineralized materials.

Subsequent HAADF-STEM analysis of the biomineralized materials after use as a CO oxidation catalyst, Figures S8 and S9, demonstrates that both ceria and ceria−zirconia particles maintain their fluorite crystal structure. Particle size distribution analysis (Figure S10) demonstrates some limited particle size growth after use as a catalyst. However, it is worth noting that a smaller increase in average particle size was found for the ceria−zirconia nanocrystals, confirming the expected increased thermal stability of ceria upon doping with zirconium.[8] This increase in average particle size is likely due to the relatively high temperature (500 °C) oxidative pretreatment conducted prior to the catalytic function tests.

While this high-temperature treatment removes some of the particle size advantage gained from low-temperature synthesis, it is necessary to fully clean the catalyst surface in this laboratory-scale catalysis demonstration. In application, however, this higher temperature step can be performed in situ during start-up of, for example, an automotive exhaust system where the catalyst will operate above 400 °C and be exposed to the varying pO_2 environment existing in the exhaust stream. This does not negate the green production advantages of direct biomineraliza-tion in terms of removing the need for corrosive precipitants or the multistep processing typically necessary to generate such small ceria−zirconia particles. Finally, the biomineralized materials described here can be utilized without the need for this high-temperature step in other applications, for instance as a biological antioxidant[67] or in chemical mechanical planarization,[68] which do not operate at high temperatures. Further process development is required to be able to controllably tune the Ce:Zr ratio in the final mixed oxide product and to recycle or reuse the enzyme to enable nanoparticle production at commercially viable levels. One possible option is to explore surface immobilization of the engineered silicatein as previously demonstrated by Tremel et al. for titania and zirconia mineralization.[31]

CONCLUSION

In summary, the demonstrated retention of crystallinity, enhanced reducibility, better CO oxidation activity, and enhanced thermal stability noted after zirconium incorporation into ceria all serve as confirmation that f unctional mixed oxide ceria−zirconia nanocrystals can be successfully prepared by our direct biomineralization route. Both the pure ceria and ceria−zirconia nanoparticles produced via our rCeSi enzymatic route exhibit catalytic performance characteristics that make them competitive with counterpart materials made by more conventional chemical methods. In addition, the much smaller particle sizes that are readily accessible via direct biomineralization can already potentially offer surface area advantages for catalysis applications and also allow fine-tuning of the band gap by quantum confinement for optical applications. Most importantly, we have conclusively demonstrated that enzymatic direct biomineralization is a viable environmentally benign route for the controlled, low-temperature, aqueous synthesis of catalytically active functional oxide nanomaterials.

EXPERIMENTAL SECTION

An E. coli codon-optimized, truncated form of silicatein from P. f iciformis (NCBI accession number Q6YD92.1) containing amino acids 124−217 with mutation T10L and added C-terminal hexahistidine tag was subcloned into plasmid pET28a as a BamHI-XhoI fragment; this adds an N-terminal hexahistidine sequence present in pET28a. Unless otherwise stated, standard molecular biology techniques were used for subclon-ing, and sequences were confirmed using standard DNA sequencing (Genscript). The resultant protein sequence is given below:

```
          10         20         30         40         50         60
HHHHHHSSGL VPRGSHMASM TGGQQMGRGS GASYAFSAMG ALEGANALAK GNAVSLSEQN

          70         80         90        100        110        120
IIDCSIPYGN HGCHGGNMYD AFLYVIANEG VDQDSAYPFV GKQSSCNYNS KYKGTSMSGM

         130        140        150        160        170        180
VSIKSGSESD LQAAVSNVGP VSVAIDGANS AFRFYYSGVY DSSRCSSSSL NHAMVVTGYG

         190        200        210        220
SYNGKKYWLA KNSWGTNWGN SGYVMMARNK YNQLEHHHHH H
```

The modified silicatein was expressed from E. coli BL21(DE3) pLysS cells using isopropyl β-D-1-thiogalactopyranoside induction, and the recombinant enzyme purified using immobilized metal affinity chromatography (IMAC) according to previously described methods.[69,70] A series of 3 × 3 h dialysis steps (Thermo Scientific Snakeskin 3.5 kDa MWCO) against DI water was used to remove residual salts from IMAC purification before use.

Particle synthesis was induced by adding either (i) 2 mM cerium ammonium nitrate (Alfa Aesar), (ii) 2 mM zirconium dinitrate oxide hydrate (Alfa Aesar), or (iii) a mixture of 1 mM cerium ammonium nitrate and 1 mM zirconium dinitrate oxide hydrate to the purified protein solution (4 μM silicatein). Samples were then incubated on an orbital shaker at room temperature. After 24 h the samples were centrifuged (18000g) for 10 min, and the pellet was resuspended in 2 mM

nitric acid solution (Fisher Scientific). This washing process was repeated five times. As reported by Patil et al. the zeta potential of ceria nanoparticles increases at lower pH, enabling the formation of a stable nanoparticle sol in dilute nitric acid without the need for an additional capping agent.[71] The samples were centrifuged and dried under vacuum prior to catalytic testing and structural characterization, as necessary. Control samples, with only the rCeSi enzyme absent, underwent exactly the same synthesis procedure as the primary samples. No indication of any particle formation or change in color occurred within 48 h.

Crystal structure and crystallite size were determined by X-ray diffraction measurements carried out at beamline 11-BM at the Advanced Photon Source, Argonne National Laboratories, USA. The diffraction spectra were collected at room temperature using incident X-rays having a wavelength of 0.414 17 Å. Rietveld refinement was conducted on as-synthesized samples utilizing GSAS[39] with the EXPGUI interface.[72] Both structures were fit to the fluorite phase, space group $Fm\bar{3}m$, with lattice parameter and Lorentzian isotropic strain parameter, L_X, refined in GSAS profile 3 to determine the mean crys-tallite size.

High-resolution XPS analysis (Rutgers University, Thermo Scientific K-Alpha+ XPS) of the Ce(3d), 875−925 eV, and Zr(3d), 176−196 eV, spectral windows were recorded using monochromatic Al Kα radiation at pass energies of 50 and 100 eV, respectively. A Ce^{4+} reference spectrum, matching previously reported Ce^{4+} doublet and satellite peaks,[73] was obtained from 15 to 30 nm ceria particles (Alfa Aesar). The reference Ce^{4+} spectrum was fitted to the measured spectra for the biomineralized materials and subtracted, leaving only the peaks contributed by Ce^{3+}. The integrated areas of the Ce^{3+} and Ce^{4+} peaks were used to calculate the relative Ce^{3+}:Ce^{4+} ratios, using a method similar to that described in a previous report.[61] The spectra were calibrated to the C(1s) line of adventitious C at 284.8 eV. Prior to XPS analysis samples were annealed at 450 °C in air.

The samples were analyzed in an aberration-corrected JEOL ARM 200CF analytical electron microscope equipped with a JEOL Centurio SDD XEDS system operating at 200 kV. Images were collected in both the high-angle annular dark field scanning transmission electron microscopy (HAADF-STEM) mode and HR-TEM modes. Samples were prepared by drop casting the aqueous sol onto carbon-coated copper mesh TEM grids. Particle size distributions from more than 50 particles were captured in HAADF-STEM images. The crystallog-raphy of individual nanoparticles was analyzed by measuring the interplanar spacings and angles from the fast Fourier transforms (FFTs) derived from the corresponding atomic resolution HAADF-STEM and HR-TEM lattice images. The lattice fringe spacings and interplanar angles were also analyzed to determine the particle orientation and identity of the exposed profile view surface facets with the most likely 3D particle shapes proposed by comparison with literature reports.[74]

X-ray energy-dispersive spectroscopy was conducted on the TEM specimens in STEM mode. When analyzing nanoparticles in the mixed oxide samples, the electron beam (probe current: 100 pA) was rastered over small rectangular regions (area: 10−75 nm^2) that enclosed groups of three or fewer particles. Collecting X-rays from small groups of particles rather than from single particles increases the signal-to-noise ratio and alleviates the amorphization and shrinkage of nanocrystals (each consisting of only a few hundred atoms) via knock-on damage during acquisition. Quantification of the XEDS spectra was carried out via the Thermo NORAN System SIX (NSS) software using the Cliff−Lorimer method.[75]

The direct optical band gap of the nanoparticles in our sols was determined from ultraviolet−visible (UV−vis) absorbance spectra measured on a Shimadzu UV-2600 spectrometer operating at room temperature over the 200−550 nm wavelength range.[76] Raman spectra were collected using a Witec alpha300RA (Knoxville, TN, USA) confocal Raman microscope with laser excitation of 532 nm. Measure-ments were performed with a spot size of ~5 um using a 20× objective. Spectra were collected using a UHTS 400NIR spectrometer with a grating of 2400 lines/mm.

The biomineralized ceria and ceria−zirconia materials were used as catalysts for carbon monoxide oxidation. Their performance was compared to that of a conventionally prepared commercial CeO_2 material (Alfa Aesar) composed of 15−30 nm particles. In order to isolate the biomineralized ceria and ceria−zirconia particles from residual enzyme, the samples were heated in air at 500 °C for 20 min (ramp rate 10 °C/min). For catalytic testing purposes, the ceria and ceria−zirconia materials were dispersed (10 wt %) onto 110 μm γ-phase alumina particles (Alfa Aesar) by mixing in ethanol. A 70 mg amount of supported catalyst was packed into a 4 mm diameter quartz reactor tube and held in place with quartz wool plugs. Prior to commencing catalysis measurements, pure oxygen was flowed through the reactor and the temperature was ramped at 10 °C/min from 30 °C to 500 °C. Gas analysis during catalytic reactions was performed using a Cirrus 2 benchtop atmospheric pressure gas analysis system (MKS Instruments). Signals for m/z = 28, 32, and 44 were monitored and assigned to CO, O_2, and CO_2, respectively. The reaction gas consisted of 2% CO, 8% O_2, and 90% Ar, and the total flow rate used was 37.5 mL/min. The reactor temperature was ramped up at 10 °C min from 30 °C to 500 °C. The procedure was repeated for each sample by cooling in pure oxygen from 500 °C to room temperature and repeating the temperature ramp in the CO-containing gas mixture.

AUTHOR INFORMATION

Corresponding Authors

*E-mail: berger@lehigh.edu.

*E-mail: mcintosh@lehigh.edu.

ORCID

Li Lu: 0000-0002-6688-1176

Steven McIntosh: 0000-0003-4664-2028

Notes

The authors declare no competing financial interest.

ACKNOWLEDGMENTS

The material presented is the result of research work supported by the National Science Foundation under the EFRI-PSBR program, Grant No. 1332349. Additional support was received from the Lehigh University Accelerator Program. Use of the Advanced Photon Source at Argonne National Laboratory was supported by the U.S. Department of Energy, Office of Science, Office of Basic Energy Sciences, under Contract No. DE-AC02-06CH11357.

REFERENCES

(1) Yao, H. C.; Yao, Y. F. Y. Ceria in Automotive Exhaust Catalysts: Oxygen Storage. J. Catal. 1984, 86, 254−265.

(2) McIntosh, S.; Gorte, R. J. Direct Hydrocarbon Solid Oxide Fuel Cells. Chem. Rev. 2004, 104, 4845−4865.

(3) Celardo, I.; Pedersen, J. Z.; Traversa, E.; Ghibelli, L. Pharmacological Potential of Cerium Oxide Nanoparticles. Nanoscale 2011, 3, 1411−1420.

(4) Krishnan, M.; Nalaskowski, J. W.; Cook, L. M. Chemical Mechanical Planarization: Slurry Chemistry, Materials, and Mecha-nisms. Chem. Rev. 2009, 110, 178−204.

(5) Zhou, K. B.; Wang, X.; Sun, X. M.; Peng, Q.; Li, Y. D. Enhanced Catalytic Activity of Ceria Nanorods from Well-Defined Reactive Crystal Planes. J. Catal. 2005, 229, 206−212.

(6) Sun, C.; Li, H.; Chen, L. Nanostructured Ceria-Based Materials: Synthesis, Properties, and Applications. Energy Environ. Sci. 2012, 5, 8475−8505.
(7) Si, R.; Flytzani-Stephanopoulos, M. Shape and Crystal-Plane Effects of Nanoscale Ceria on the Activity of Au-CeO_2 Catalysts for the Water-Gas Shift Reaction. Angew. Chem., Int. Ed. 2008, 47, 2884−2887.
(8) Mamontov, E.; Egami, T.; Brezny, R.; Koranne, M.; Tyagi, S. Lattice Defects and Oxygen Storage Capacity of Nanocrystalline Ceria and Ceria-Zirconia. J. Phys. Chem. B 2000, 104, 11110−11116.
(9) Bunluesin, T.; Gorte, R. J.; Graham, G. W. CO Oxidation for the Characterization of Reducibility in Oxygen Storage Components of Three-Way Automotive Catalysts. Appl. Catal., B 1997, 14, 105−115.
(10) Stark, W. J.; Madler, L.; Maciejewski, M.; Pratsinis, S. E.; Baiker, A. Flame Synthesis of Nanocrystalline Ceria-Zirconia: Effect of Carrier Liquid. Chem. Commun. 2003, 5, 588−589.
(11) Escribano, V. S.; Lopez, E. F.; Panizza, M.; Resini, C.; Amores, J. M. G.; Busca, G. Characterization of Cubic Ceria-Zirconia Powders by X-ray Diffraction and Vibrational and Electronic Spectroscopy. Solid State Sci. 2003, 5, 1369−1376.
(12) Lee, J. S.; Choi, S. C. Crystallization Behavior of Nano-Ceria Powders by Hydrothermal Synthesis Using a Mixture of H_2O_2 and NH_4OH. Mater. Lett. 2004, 58, 390−393.
(13) Heuer, A. H.; Fink, D. J.; Laraia, V. J.; Arias, J. L.; Calvert, P. D.; Kendall, K.; Messing, G. L.; Blackwell, J.; Rieke, P. C.; Thompson, D. H.; Wheeler, A. P.; Veis, A.; Caplan, A. I. Innovative Materials Processing Strategies: a Biomimetic Approach. Science 1992, 255, 1098−1105.
(14) Nudelman, F.; Sommerdijk, N. A. J. M. Biomineralization as an Inspiration for Materials Chemistry. Angew. Chem., Int. Ed. 2012, 51, 6582−6596.
(15) Addadi, L.; Raz, S.; Weiner, S. Taking Advantage of Disorder: Amorphous Calcium Carbonate and its Roles in Biomineralization. Adv. Mater. 2003, 15, 959−970.
(16) St Pierre, T. G.; Mann, S.; Webb, J.; Dickson, D. P. E.; Runham, N. W.; Williams, R. J. P. Iron Oxide Biomineralization in the Radula Teeth of the Limpet Patella vulgata; Mossbauer Spectroscopy and High Resolution Transmission Electron Microscopy Studies. Proc. R. Soc. London, Ser. B 1986, 228, 31−42.
(17) Cha, J. N.; Shimizu, K.; Zhou, Y.; Christiansen, S. C.; Chmelka, B. F.; Stucky, G. D.; Morse, D. E. Silicatein Filaments and Subunits from a Marine Sponge Direct the Polymerization of Silica and Silicones In Vitro. Proc. Natl. Acad. Sci. U. S. A. 1999, 96, 361−365.
(18) Mann, S. Biomineralization: Principles and Concepts in Bioinorganic Materials Chemistry; Oxford Univ. Press: Oxford, 2001; Vol. 5.
(19) Spoerke, E. D.; Voigt, J. A. Influence of Engineered Peptides on the Formation and Properties of Cadmium Sulfide Nanocrystals. Adv. Funct. Mater. 2007, 17, 2031−2037.
(20) Rosant, C.; Avalle, B.; Larcher, D.; Dupont, L.; Friboulet, A.; Tarascon, J. Biosynthesis of Co_3O_4 Electrode Materials by Peptide and Phage Engineering: Comprehension and Future. Energy Environ. Sci. 2012, 5, 9936−9943.
(21) Okuda, M.; Suzumoto, Y.; Yamashita, I. Bioinspired Synthesis of Homogenous Cerium Oxide Nanoparticles and Two- or Three-Dimensional Nanoparticle Arrays Using Protein Supramolecules. Cryst. Growth Des. 2011, 11, 2540−2545.
(22) Dunleavy, R.; Lu, L.; Kiely, C. J.; McIntosh, S.; Berger, B. W. Single-Enzyme Biomineralization of Cadmium Sulfide Nanocrystals with Controlled Optical Properties. Proc. Natl. Acad. Sci. U. S. A. 2016, 113, 5275−5280.
(23) Shimizu, K.; Cha, J.; Stucky, G. D.; Morse, D. E. Silicatein Alpha: Cathepsin L-like Protein in Sponge Biosilica. Proc. Natl. Acad. Sci. U. S. A. 1998, 95, 6234−6238.
(24) Brutchey, R. L.; Morse, D. E. Silicatein and the Translation of its Molecular Mechanism of Biosilicification into Low Temperature Nanomaterial Synthesis. Chem. Rev. 2008, 108, 4915−4934.
(25) Andre, R.; Tahir, M. N.; Natalio, F.; Tremel, W. Bioinspired Synthesis of Multifunctional Inorganic and Bio-organic Hybrid Materials. FEBS J. 2012, 279, 1737−1749.
(26) Sumerel, J. L.; Yang, W. J.; Kisailus, D.; Weaver, J. C.; Choi, J. H.; Morse, D. E. Biocatalytically Templated Synthesis of Titanium Dioxide. Chem. Mater. 2003, 15, 4804−4809.
(27) Kisailus, D.; Choi, J. H.; Weaver, J. C.; Yang, W. J.; Morse, D. E. Enzymatic Synthesis and Nanostructural Control of Gallium Oxide at Low Temperature. Adv. Mater. 2005, 17, 314−318.
(28) Andre, R.; Tahir, M. N.; Schröder, H. C. C.; Müller, W. E.; Tremel, W. Enzymatic Synthesis and Surface Deposition of Tin Dioxide Using Silicatein-α. Chem. Mater. 2011, 23, 5358−5365.
(29) Brutchey, R. L.; Yoo, E. S.; Morse, D. E. Biocatalytic Synthesis of a Nanostructured and Crystalline Bimetallic Perovskite-like Barium Oxofluorotitanate at Low Temperature. J. Am. Chem. Soc. 2006, 128, 10288−10294.
(30) Andre, R.; Tahir, M. N.; Link, T.; Jochum, F. D.; Kolb, U.; Theato, P.; Berger, R.; Wiens, M.; Schröder, H.; Müller, W. E. Chemical Mimicry: Hierarchical 1D TiO_2@ ZrO_2 Core−Shell Structures Reminiscent of Sponge Spicules by the Synergistic Effect of Silicatein-α and Silintaphin-1. Langmuir 2011, 27, 5464−5471.
(31) Tahir, M. N.; Theato, P.; Muller, W. E.; Schroder, H. C.; Borejko, A.; Faiß, S.; Janshoff, A.; Huth, J.; Tremel, W. Formation of Layered Titania and Zirconia Catalysed by Surface-Bound Silicatein. Chem. Commun. 2005, 5533−5535.
(32) Tahir, M. N.; Eberhardt, M.; Therese, H. A.; Kolb, U.; Theato, P.; Müller, W. E.; Schröder, H.; Tremel, W. From Single Molecules to Nanoscopically Structured Functional Materials: Au Nanocrystal Growth on TiO_2 Nanowires Controlled by Surface-Bound Silicatein. Angew. Chem., Int. Ed. 2006, 45, 4803−4809.
(33) Bawazer, L. A.; Izumi, M.; Kolodin, D.; Neilson, J. R.; Schwenzer, B.; Morse, D. E. Evolutionary Selection of Enzymatically Synthesized Semiconductors from Biomimetic Mineralization Vesicles. Proc. Natl. Acad. Sci. U. S. A. 2012, 109, E1705−E1714.
(34) Spangler, L. C.; Lu, L.; Kiely, C. J.; Berger, B. W.; McIntosh, S. Biomineralization of PbS and PbS−CdS Core−Shell Nanocrystals and Their Application in Quantum Dot Sensitized Solar Cells. J. Mater. Chem. A 2016, 4, 6107−6115.
(35) Bharde, A.; Rautaray, D.; Bansal, V.; Ahmad, A.; Sarkar, I.; Yusuf, S. M.; Sanyal, M.; Sastry, M. Extracellular Biosynthesis of Magnetite Using Fungi. Small 2006, 2, 135−141.
(36) Bansal, V.; Poddar, P.; Ahmad, A.; Sastry, M. Room-Temperature Biosynthesis of Ferroelectric Barium Titanate Nanoparticles. J. Am. Chem. Soc. 2006, 128, 11958−11963.
(37) Li, Q.; Liu, D.; Jia, Z.; Csetenyi, L.; Gadd, G. M. Fungal Biomineralization of Manganese as a Novel Source of Electrochemical Materials. Curr. Biol. 2016, 26, 950−955.
(38) Miot, J.; Recham, N.; Larcher, D.; Guyot, F.; Brest, J.; Tarascon, J. Biomineralized α-Fe_2O_3: Texture and Electrochemical Reaction with Li. Energy Environ. Sci. 2014, 7, 451−460.
(39) Larson, A.; Von Dreele, R. General Structure Analysis System (GSAS); Los Alamos National Laboratory: Los Alamos, NM, 2004; Report LAUR 86-748.
(40) Yu, T.; Lim, B.; Xia, Y. Aqueous Phase Synthesis of Single-Crystal Ceria Nanosheets. Angew. Chem., Int. Ed. 2010, 49, 4484−4487.
(41) Depner, S. W.; Kort, K. R.; Jaye, C.; Fischer, D. A.; Banerjee, S. Nonhydrolytic Synthesis and Electronic Structure of Ligand Capped CeO_2-delta and CeOCl nanocrystals. J. Phys. Chem. C 2009, 113, 14126−14134.
(42) Yao, M.; Baird, R.; Kunz, F.; Hoost, T. An XRD and TEM Investigation of the Structure of Alumina-Supported Ceria−Zirconia. J. Catal. 1997, 166, 67−74.
(43) Hori, C. E.; Permana, H.; Ng, K. S.; Brenner, A.; More, K.; Rahmoeller, K. M.; Belton, D. Thermal Stability of Oxygen Storage Properties in a Mixed CeO_2-ZrO_2 System. Appl. Catal., B 1998, 16, 105−117.
(44) Zhang, H. T.; Wu, G.; Chen, X. H. Thermal Stability and Photoluminescence of $Zr_{1-x}Ce_xO_2$ ($0 \le x \le 1$) Nanoparticles Synthesized in a Non-aqueous Process. Mater. Chem. Phys. 2007, 101, 415−422.
(45) Duwez, P.; Odell, F. Phase Relationships in the System Zirconia-Ceria. J. Am. Ceram. Soc. 1950, 33, 274−283.

(46) Hirano, M.; Miwa, T.; Inagaki, M. Low-Temperature Direct Synthesis of Nanoparticles of Fluorite-Type Ceria-Zirconia Solid Solutions by “Forced Cohydrolysis” at 100°C. J. Solid State Chem. 2001, 158, 112−117.

(47) Armirotti, A.; Damonte, G.; Pozzolini, M.; Mussino, F.; Cerrano, C.; Salis, A.; Benatti, U.; Giovine, M. Primary Structure and Post-translational Modifications of Silicatein Beta from the Marine Sponge Petrosia f iciformis (Poiret, 1789). J. Proteome Res. 2009, 8, 3995−4004.

(48) Guillou, N.; Auffredic, J. P.; Louer, M.; Louer, D. The Crystal Structure of Hydronium Cerium(III) Nitrate Hydrate, $Ce(NO_3)_5(H_3O)_2 \cdot H_2O$. J. Solid State Chem. 1993, 106, 295−300.

(49) Demars, T. J.; Bera, M. K.; Seifert, S.; Antonio, M. R.; Ellis, R. J. Revisiting the Solution Structure of Ceric Ammonium Nitrate. Angew. Chem., Int. Ed. 2015, 54, 7534−7538.

(50) Zhou, Y.; Shimizu, K.; Cha, J. N.; Stucky, G. D.; Morse, D. E. Efficient Catalysis of Polysiloxane Synthesis by Silicatein Alpha Requires Specific Hydroxy and Imidazole Functionalities. Angew. Chem., Int. Ed. 1999, 38, 779−782.

(51) Wang, Z. L.; Feng, X. D. Polyhedral Shapes of CeO_2 Nanoparticles. J. Phys. Chem. B 2003, 107, 13563−13566.

(52) Reddy, B. M.; Bharali, P.; Thrimurthulu, G.; Saikia, P.; Katta, L.; Park, S. Catalytic Efficiency of Ceria−Zirconia and Ceria-Hafnia Nanocomposite Oxides for Soot Oxidation. Catal. Lett. 2008, 123, 327−333.

(53) Katta, L.; Sudarsanam, P.; Thrimurthulu, G.; Reddy, B. M. Doped Nanosized Ceria Solid Solutions for Low Temperature Soot Oxidation: Zirconium Versus Lanthanum Promoters. Appl. Catal., B 2010, 101, 101−108.

(54) Luo, M.; Yan, Z.; Jin, L.; He, M. Raman Spectroscopic Study on the Structure in the Surface and the Bulk Shell of $Ce_xPr_{1-x}O_{2-\delta}$ Mixed Oxides. J. Phys. Chem. B 2006, 110, 13068−13071.

(55) Burroughs, P.; Hamnett, A.; Orchard, A. F.; Thornton, G. Satellite Structure in X-ray Photoelectron Spectra of Some Binary and Mixed Oxides of Lanthanum and Cerium. J. Chem. Soc., Dalton Trans. 1976, 17, 1686−1698.

(56) Patsalas, P.; Logothetidis, S.; Sygellou, L.; Kennou, S. Structure-Dependent Electronic Properties of Nanocrystalline Cerium Oxide Films. Phys. Rev. B: Condens. Matter Mater. Phys. 2003, 68, 035104.

(57) Yang, Z.; Wei, Y.; Fu, Z.; Lu, Z.; Hermansson, K. Facilitated Vacancy Formation at Zr-Doped Ceria (111) Surfaces. Surf. Sci. 2008, 602, 1199−1206.

(58) Yang, Z.; Woo, T. K.; Hermansson, K. Effects of Zr Doping on Stoichiometric and Reduced Ceria: a First Principles Study. J. Chem. Phys. 2006, 124, 224704.

(59) Zhang, F.; Wang, P.; Koberstein, J.; Khalid, S.; Chan, S. Cerium Oxidation State in Ceria Nanoparticles Studied with X-ray Photo-electron Spectroscopy and Absorption Near Edge Spectroscopy. Surf. Sci. 2004, 563, 74−82.

(60) Tsunekawa, S.; Ishikawa, K.; Li, Z.; Kawazoe, Y.; Kasuya, A. Origin of Anomalous Lattice Expansion in Oxide Nanoparticles. Phys. Rev. Lett. 2000, 85, 3440.

(61) Zhang, C.; Grass, M. E.; McDaniel, A. H.; DeCaluwe, S. C.; El Gabaly, F.; Liu, Z.; McCarty, K. F.; Farrow, R. L.; Linne, M. A.; Hussain, Z.; Jackson, G. S.; Bluhm, H.; Eichhorn, B. W. Measuring Fundamental Properties in Operating Solid Oxide Electrochemical Cells by Using In Situ X-ray Photoelectron Spectroscopy. Nat. Mater. 2010, 9, 944−949.

(62) Tsunekawa, S.; Fukuda, T.; Kasuya, A. Blue Shift in Ultraviolet Absorption Spectra of Monodisperse CeO_{2-x} Nanoparticles. J. Appl. Phys. 2000, 87, 1318−1321.

(63) Nahory, R.; Pollack, M.; Johnston, W., Jr; Barns, R. Band Gap Versus Composition and Demonstration of Vegard’s Law for $In_{1-x}Ga_xAs_yP_{1-y}$ Lattice Matched to InP. Appl. Phys. Lett. 1978, 33, 659−661.

(64) French, R.; Glass, S.; Ohuchi, F.; Xu, Y.; Ching, W. Experimental and Theoretical Determination of the Electronic Structure and Optical Properties of Three Phases of ZrO_2. Phys. Rev. B: Condens. Matter Mater. Phys. 1994, 49, 5133.

(65) Castleton, C.; Kullgren, J.; Hermansson, K. Tuning LDA U for Electron Localization and Structure at Oxygen Vacancies in Ceria. J. Chem. Phys. 2007, 127, 244704−244704.

(66) Nolan, M.; Parker, S. C.; Watson, G. W. The Electronic Structure of Oxygen Vacancy Defects at the Low Index Surfaces of Ceria. Surf. Sci. 2005, 595, 223−232.

(67) Kwon, H. J.; Cha, M.; Kim, D.; Kim, D. K.; Soh, M.; Shin, K.; Hyeon, T.; Mook-Jung, I. Mitochondria-Targeting Ceria Nanoparticles as Antioxidants for Alzheimer’s Disease. ACS Nano 2016, 10, 2860− 2870.

(68) Coutinho, C. A.; Mudhivarthi, S. R.; Kumar, A.; Gupta, V. K. Novel Ceria-Polymer Microcomposites for Chemical Mechanical Polishing. Appl. Surf. Sci. 2008, 255, 3090−3096.

(69) Studier, F. W. Protein Production by Auto-induction in High-density Shaking Cultures. Protein Expression Purif. 2005, 41, 207−234.

(70) Porath, J. Immobilized Metal Ion Affinity Chromatography. Protein Expression Purif. 1992, 3, 263−281.

(71) Patil, S.; Sandberg, A.; Heckert, E.; Self, W.; Seal, S. Protein Adsorption and Cellular Uptake of Cerium Oxide Nanoparticles as a Function of Zeta Potential. Biomaterials 2007, 28, 4600−4607.

(72) Toby, B. H. EXPGUI, a Graphical User Interface for GSAS. J. Appl. Crystallogr. 2001, 34, 210−213.

(73) Mullins, D. R.; Overbury, S. H.; Huntley, D. R. Electron Spectroscopy of Single Crystal and Polycrystalline Cerium Oxide Surfaces. Surf. Sci. 1998, 409, 307−319.

(74) Cordeiro, M. A. L.; Weng, W.; Stroppa, D. G.; Kiely, C. J.; Leite, E. R. High Resolution Electron Microscopy Study of Nanocubes and Polyhedral Nanocrystals of Cerium(IV) Oxide. Chem. Mater. 2013, 25, 2028−2034.

(75) Cliff, G.; Lorimer, G. W. The Quantitative Analysis of Thin Specimens. J. Microsc. 1975, 103, 203−207.

(76) Tauc, J.; Grigorovici, R.; Vancu, A. Optical Properties and Electronic Structure of Amorphous Germanium. Phys. Status Solidi B 1966, 15, 627−637.